

## The fabric of consolidation in Gulf of Mexico mudstones

Ruarri J. Day-Stirrat<sup>a,\*</sup>, Peter B. Flemings<sup>b</sup>, Yao You<sup>b</sup>, Andrew C. Aplin<sup>c</sup>, Ben A. van der Pluijm<sup>d</sup>

<sup>a</sup> Bureau of Economic Geology, Jackson School of Geosciences, The University of Texas at Austin, University Station, Box X, Austin, TX, 78713, USA

<sup>b</sup> Jackson School of Geosciences, The University of Texas at Austin, University Station, Box X, Austin, TX, 78713, USA

<sup>c</sup> School of Civil Engineering and Geosciences, Drummond Building, Newcastle University, Newcastle upon Tyne, NE1 7RU, UK

<sup>d</sup> Department of Geological Sciences, University of Michigan, C.C. Little Building, 425 E. University Ave., Ann Arbor, MI 48109, USA

### ARTICLE INFO

#### Article history:

Received 22 August 2011

Received in revised form 1 December 2011

Accepted 9 December 2011

Available online 26 December 2011

#### Keywords:

high resolution X-ray texture goniometry

anisotropy

mudstone porosity

preferred orientation

clay mineral

### ABSTRACT

How the micro-scale fabric of clay-rich mudstone evolves during consolidation in early burial is critical to how they are interpreted in the deeper portions of sedimentary basins. Core samples from the Integrated Ocean Drilling Program Expedition 308, Ursa Basin, Gulf of Mexico, covering seafloor to 600 meters below sea floor (mbsf) are ideal for studying the micro-scale fabric of mudstones. Mudstones of consistent composition and grain size decrease in porosity from 80% at the seafloor to 37% at 600 mbsf. Argon-ion milling produces flat surfaces to image this pore evolution over a vertical effective stress range of 0.25 (71 mbsf) to 4.05 MPa (597 mbsf). With increasing burial, pores become elongated, mean pore size decreases, and there is preferential loss of the largest pores. There is a small increase in clay mineral preferred orientation as recorded by high resolution X-ray goniometry with burial.

© 2011 Elsevier B.V. All rights reserved.

### 1. Introduction

Clay-rich sediments undergo a remarkable volume loss in the first kilometer below seafloor as effective stress increases. This volume loss has been described by a variety of empirical equations (e.g. Athy, 1930; Hedberg, 1936; Rubey and Hubbert, 1959; Sclater and Christie, 1980; Baldwin and Butler, 1985; Long et al., 2011). It has long been held that rotation of randomly aligned clay floccules ('house of cards') to a layered ('deck of cards') structure allows the enormous volume loss and generates the preferred orientation that is observed at depth.

Previous X-ray based clay mineral preferred orientation studies have concentrated on fault gouge (Solum et al., 2005; Solum and van der Pluijm, 2009), metamorphic grade (Jacob et al., 2000), silt-to-clay ratios in late-diagenesis (Curtis et al., 1980; Day-Stirrat et al., 2010) and the smectite to illite transformation (Ho et al., 1999; Day-Stirrat et al., 2008), yet none have systematically captured the first kilometer of burial in modern sediments.

Despite the importance of porosity evolution in shallow burial in predicting pressure from porosity (Hart et al., 1995; Long et al., 2011) or the onset of permeability anisotropy (Arch and Maltman, 1990), there are few detailed examinations of the gross fabric of consolidation at the micro-scale. There is remarkable similarity in

the composition and texture of Ursa mudstones from the seafloor to over 600 meters of depth and this allows a detailed examination of the evolution of consolidation free from significant grain-size heterogeneity that can plague micro-fabric study. We substitute space for time and infer that deeper samples record the evolution of consolidation relative to the shallower samples. This paper describes pore size and shape, provides images of pore evolution at various stages of consolidation, and documents, as a function of increasing vertical effective stress, clay particle rotation. This study has significant implications for the development of permeability anisotropy in shallow systems (Arch and Maltman, 1990) as pore shape change and pore throat size evolution are systematically documented. Projection of mechanical properties from shallow to greater depth (Ask and Morgan, 2010) do not take into account particle reorientation and pore flattening. In a similar fashion, models that describe the evolution of velocity anisotropy with compaction do not consider particle re-orientation or pore flattening (Domnesteau et al., 2002).

### 2. Materials and methods

#### 2.1. Ursa region samples

Whole cores from IODP Expedition 308 Site 1324 and Site 1322 (Fig. 1) provide the samples for this study. Mass transport deposits (MTDs) are frequently encountered at Ursa (Sawyer et al., 2009). However, care was taken to select sample not impacted by mass movement. Samples range from depths of 71.5 to 579.6 mbsf (Fig. 2, Table 1). In order to achieve this coverage, both sites U1324 and U1322 were sampled. The four shallowest samples (71.5–149.9

\* Corresponding author at: Shell International Exploration and Production, Projects and Technology, 3737 Bellaire Boulevard, Houston, Texas, 77025, USA. Tel.: +1 713 245 7681.

E-mail address: [ruarri.day-stirrat@shell.com](mailto:ruarri.day-stirrat@shell.com) (R.J. Day-Stirrat).

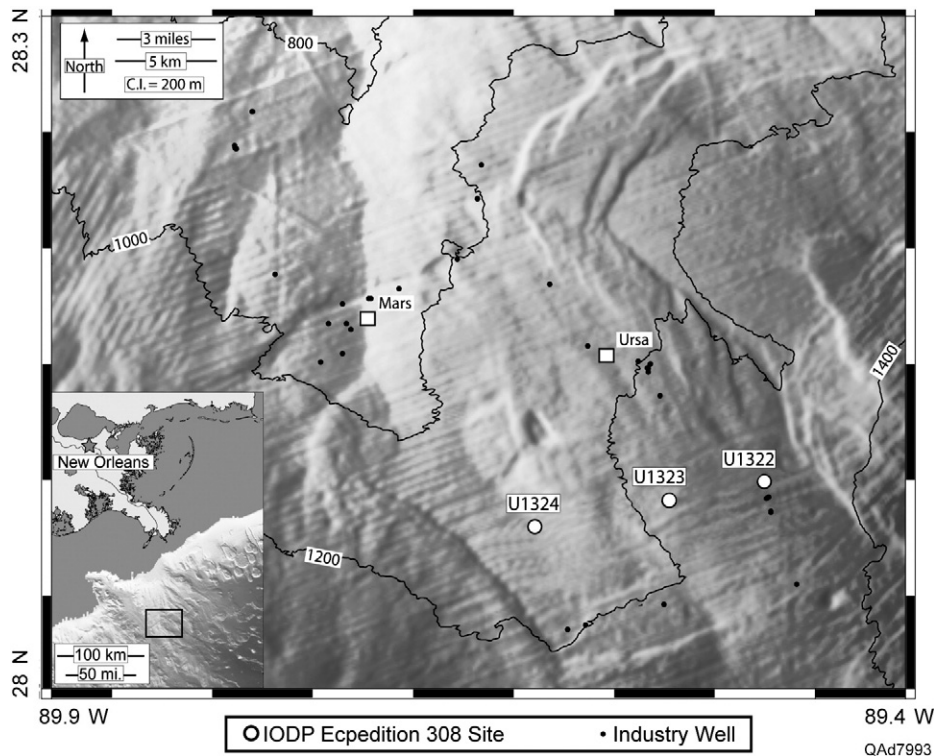


**Fig. 1.** The location of the Ursa Basin on the continental slope in water depths of ~1000 m. The Ursa Basin in the Gulf of Mexico and the locations of IODP Expedition Leg 308 drill sites U1234, U1323 and U1322 relative to Oil and Gas drilling platforms Mars and Ursa.

mbsf) come from U1322 (Table 1). Sediments in this shallow section have a similar composition and depositional history at both Site U1322 and U1324 (Flemings et al., 2006; Sawyer et al., 2009). From 178.6 to 579.6 mbsf, samples are derived from Site U1324 (Table 1).

## 2.2. Porosimetry

Pore throat size distributions on 7 samples from Site 1324 and 4 samples at Site 1322 (Table 1) were determined by mercury porosimetry. For each analysis a one gram block of mudstone sample was submerged in liquid nitrogen for 5 minutes before being freeze dried (Delage and Lefebvre, 1984) for 24 hours, then dried in an oven at 105°C for a further 24 hours. Freeze-drying effectively eliminate surface tension forces and, therefore, no shrinkage of the sample by the dehydration of illite-smectite is expected in sample preparation (Romero and Simms, 2008). The porosity of each sample was calculated from dry bulk density ( $\rho_d$ ) and grain density ( $G_s$ ):

$$\phi = 1 - \frac{\rho_d}{G_s} \quad (1)$$

Grain density was determined previously for Ursa region samples and was generally near 2.70 g/cm<sup>3</sup> (Sawyer et al., 2008). Therefore, grain density was assumed to be 2.70 g/cm<sup>3</sup> in the above calculation. Small differences in actual grain densities relative to the assumed values can increase or decrease porosity by a tiny amount and move the small pore size tail of a pore throat size distribution up or down by a small margin, but are not significant in this study. Dry bulk density ( $\rho_d$ ) was calculated from the known mass of the sample after drying and from the bulk volume of the sample measured in the mercury penetrometer.

During mercury intrusion experiments, mercury is injected at a progressively increasing pressure into the dried and evacuated sample (e.g. Arnould et al., 1980; Lowell and Shields, 1984). The mercury

pressure is assumed to equal the capillary pressure in the smallest pore throats that the mercury can enter. The radius ( $r$ ) of the pore throats can thus be inferred from the Young-Laplace equation:

$$r = 2\gamma(\cos\theta)/P \quad (2)$$

To calculate the pore throat radius ( $r$ ) from absolute mercury injection pressure ( $P$ ), it is assumed that the surface tension of mercury ( $\gamma$ ) is 0.48 N/m and the contact angle between mercury and the particle surface ( $\theta$ ) is 141° (e.g. Hildenbrand and Urai, 2003). To use Eq. (2) to infer pore throat distribution, all pore throats must be accessible to the mercury as in, for example, a parallel capillary tube model (e.g. Schowalter, 1979; Romero and Simms, 2008).

## 2.3. Preferred orientation

The maximum X-ray diffraction peak close to a d-spacing of 10 Å, corresponding to 001 peak of illite-smectite, was analyzed to assess illite-smectite preferred orientation on an Enraf-Nonius CAD4 automated single-crystal diffractometer using the high resolution X-ray texture goniometry (HRXTG) method described by van der Pluijm et al. (1994). The peak close to 10 Å (illite-smectite) was analyzed for all samples and, where present, a 7 Å peak was analyzed which corresponds to the overlapping 001 peak of kaolinite and 002 peak of chlorite. Lower hemisphere equal area projections of X-ray intensity at different tilt and rotation angles were used to assess data quality and described only minimal data lost to an unmeasured area (van der Pluijm et al., 1994; Sintubin, 1995; van der Pluijm et al., 1995). The degree of clay mineral preferred orientation is expressed as maximum pole densities in, m.r.d., multiples of a random distribution (Wenk, 1985), in which higher values reflect higher degrees of preferred orientation.

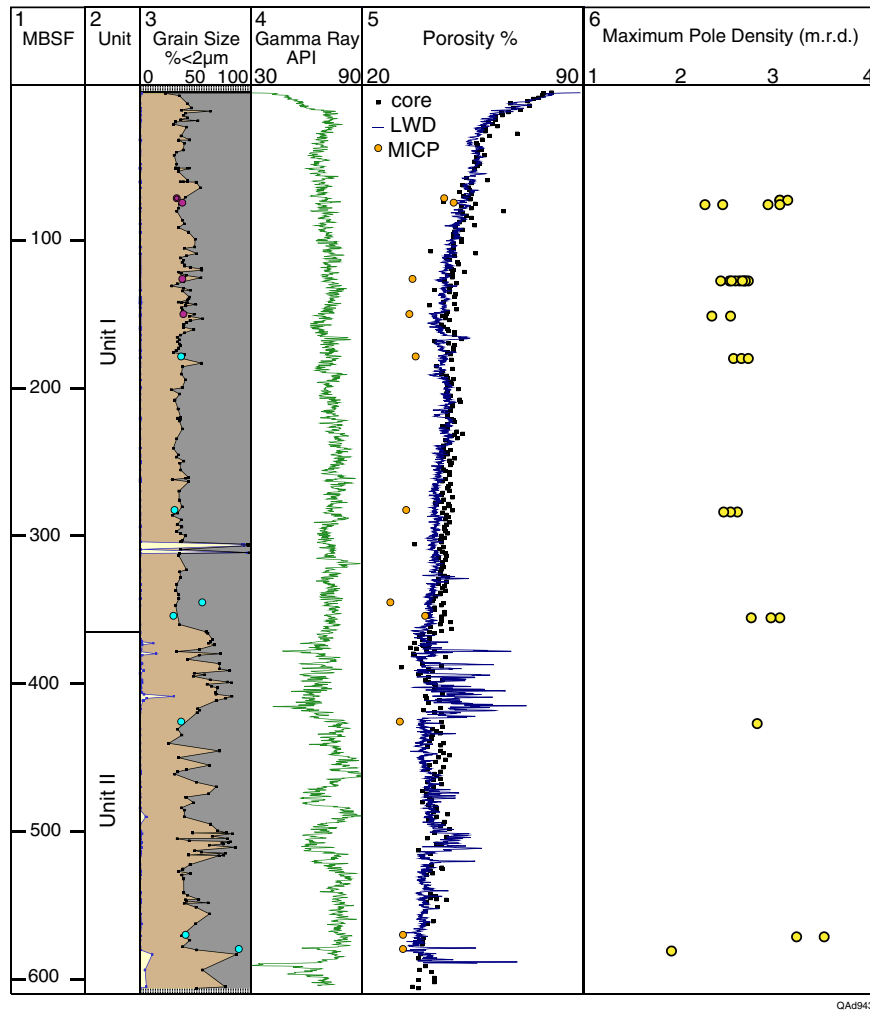


**Fig. 2.** IODP Site 1324. 1) Depth in meters below sea floor. 2) Units I and II were defined during IODP Expedition 308 drilling (Flemings et al., 2006). 3) Sand sized fraction (> 64  $\mu\text{m}$ ) shown in yellow, silt-sized fraction shown in brown, clay-sized fraction (< 2  $\mu\text{m}$ ) shown in grey. Blue circles represent the percent of silt plus sand for additional analyses in this study. 4) Gamma-ray log response (gapi units). 5) Porosity (%) from core (moisture and density), logging (LWD = logging while drilling) and mercury injection (MICP). 6) illite-smectite maximum pole density (preferred orientation) in multiples of a random distribution (m.r.d.). The first four samples (red circles) are from Site 1322 and projected onto the 1324 location.

#### 2.4. Pore and particle imaging

A subsample, adjacent to that prepared for HRXTG, was cut for backscattered electron microscopy (BSE). Argon-ion milling - produces surfaces, cut approximately perpendicular to bedding, that show only minor topographic relief unrelated to differences in mineral hardness. The Argon-ion milling system was operated at an accelerating voltage of 5 to 7 kV and a gun current of ~300  $\mu\text{A}$ . These settings have proven effective at producing relatively flat surfaces for imaging pores (Loucks et al., 2009). Samples were examined using a Zeiss Supra 40 VP field emission SEM and an SE detector, at the University of Texas, using an accelerating voltage of 10 kV and a working distance of ~5 mm.

#### 2.5. Grain size

Grain size distributions were analyzed using the standard hydrometer method (ASTM, 2007). Grain density for the hydrometer analysis was previously determined for Ursa region samples (Sawyer et al., 2008) according to ASTM Standard D854-06 (ASTM, 2007), which is a water pycnometer method. Eleven grain sizes were determined for this study (Table 1).

### 3. Results

#### 3.1. Lithology

Grain size, gamma-ray (GR) log response, (Sawyer et al., 2009) and mineralogy (John and Adatte, 2009) do not vary significantly within mudstones at Ursa (Fig. 2.3, 2.4). Four XRD measurements on samples from Ursa show a clay mineralogy dominated by illite-smectite (Table 2) but also the presence of kaolinite and chlorite. At site U1324, Unit 1 is composed of mudstone while the underlying Unit II is composed of interbedded mudstones and siltstones (Fig. 2.2). Samples from Units I and II that had similar gamma-ray log response and a clay-sized fraction (less than 2 micrometers) of approximately 65% (Fig. 2) were selected for analysis. Mudstones within Unit 1 and Unit II have a fairly homogenous mineralogical composition even though Unit II contains more silt-rich beds. Generally, within Unit 1 (0–300 mbsf), the quartz content by mass is constant (~25%) whereas beneath this it increases to 30%, but with some heterogeneity (John and Adatte, 2009). Potassium feldspar also increases from 2 to 5% and sodium plagioclase increases from 5 to 8% beneath 300 mbsf. Total phyllosilicate content (clay) decreases from 45% at the top to 30% at the bottom of the hole, with



**Table 2**Bulk mineralogy (Weight %) by the Reference Intensity Ratio method and the relative % of clay minerals in the <2  $\mu\text{m}$ .

Bulk Mineralogy (Weight %) by RIR Method												
Sample	Depth	Quartz	Plagioclase	K-Feldspar	Calcite	Dolomite	Siderite	Pyrite	Halite	Gypsum	Amphibole	Clinoptilite
U1322D002H02WR	71.5	18.8	5.6	4	7.5	6.7	1.9	0.4	0.4	0	0	1.3
U1322D002H04WR	74.5	21.6	6.9	5.2	4.6	7.4	1.1	0.7	0.5	0	0	0
U1324B020H06WR	178.7	20.1	8.2	6.8	11	16	1.7	0.5	0	0	1.3	0
U1324B044H01WR	354.1	20.8	10.5	7.3	4.7	11.3	1.5	0	0	0	2.4	0
Sample	Depth	Muscovite	Illite + Illite-smectite	Kaolinite	Chlorite	Tri-mica	Hydrobiotite	Talc	Total Clay	Total Carbonate	Total Qtz + Feld	Total
U1322D002H02WR	71.5	5	42.4	3.5	2.3	0	0	0.5	53.7	16.5	28.4	100.3
U1322D002H04WR	74.5	4.5	40.8	3.9	2.9	0	0	0	52.1	13.6	33.7	100.1
U1324B020H06WR	178.7	4.7	25.4	0.7	3.6	0	0	0	34.4	28.7	35.1	100
U1324B044H01WR	354.1	4.3	29.7	3.9	3.6	0	0	0	41.5	17.5	38.6	100
Relative % of clay minerals in <2 $\mu\text{m}$ clay size												
Sample	Depth	Chlorite	Kaolinite	Illite	Illite-smectite	%Expandibility						
U1322D002H02WR	71.5	2	2	16	80	85						
U1322D002H04WR	74.5	4	4	21	72	85						
U1324B020H06WR	178.7	7	4	28	60	75						
U1324B044H01WR	354.1	7	8	17	68	75						

heterogeneity driven by calcite and dolomite content variations (John and Adatte, 2009). Although Unit II becomes more sand-rich, in almost all cases we chose samples with consistent clay contents (Table 1) and mineralogy (Table 2).

### 3.2. Porosity

Long et al. (2011) described the porosity in mudstones at IODP Site U1324 and IODP Site U1322. At Site U1324 (Fig. 2.5) porosity declines from 80% at the seafloor to 37% at 612 mbsf. Core-derived porosities from moisture and density (MAD) are typically ~2% greater than logging while drilling (LWD) derived porosities (Fig. 2.5); this is because the core expands when it is removed from the borehole. In turn, porosity calculated from mercury injection (MICP) is consistently about 5 porosity units lower than Logging While Drilling (LWD) porosity (Fig. 2.5). Shrinkage of the sample during storage and transport causes this discrepancy. In addition, clay-bound water is interpreted as porosity in both LWD and MAD data. However, this is not pore water and cannot be accessed by mercury.

### 3.3. Clay mineral preferred orientation

Illite-smectite maximum pole density (in m.r.d.) increases, approximately linearly, from ~2.24 at 71.5 mbsf to ~3.45 at the bottom of the hole (Fig. 2.6). The deepest sample, at 579 mbsf, has a much lower maximum pole density, but is also silt-rich (clay fraction = 20%) (Fig. 2.3, Table 1). Multiple measurements on the same sample document heterogeneity in the illite-smectite preferred orientation (Fig. 2) on a millimeter scale, the diameter of the X-ray beam.

### 3.4. Pore and particle images

Back-scattered electron (BSE) images for three samples (Fig. 3) located at 74.5 mbsf ( $\sigma_v = 0.25$  MPa), 178.6 mbsf ( $\sigma_v = 0.90$  MPa) and 570.0 mbsf ( $\sigma_v = 3.98$  MPa) cover the depth and stress range in this study. These samples have a porosity of 49, 37 and 31 percent as measured by the MICP analyses, respectively (Fig. 4, Table 1). The largest pores are adjacent to the largest (~5  $\mu\text{m}$  diameter) silt particles (refer to Fig. 3) and in one example (Fig. 3a) clay particles appear molded onto the surface of a quartz grain (similarly noted by Forsberg and Locat, 2005) with an associated rim of clay-micropores. Smaller pores are also preserved between clay-sized particles. Silt-sized grains bridge smaller grains and form stress arches providing a

location where porosity may be preserved. The preferential loss of large pores can be seen with increasing stress (Fig. 3). There is an array of pore shapes preserved in Ursa mudstones, some being quite rounded others more oblate but both somewhat evenly distributed around the image. With increased vertical effective stress the general shape of pores evolves from angular or rounded to more elongate forms (Fig. 3). These samples have an increase in illite-smectite maximum pole density from ~2.2 m.r.d. at 71.5 mbsf to ~3.4 m.r.d. at 570 mbsf. It does appear that the deeper sample has more horizontal alignment than the shallowest sample both in terms of pore flattening and particle orientation (Fig. 3).

### 3.5. Pore throat size

The pore evolution recorded in BSE images on Argon ion-milled samples is captured quantitatively in the cumulative porosity curves (Fig. 4a) generated from mercury porosimetry. With increasing effective stress, the total porosity decreases from 49% to 31% while the median pore size decreases from 156 nm to 37 nm (Fig. 4, Table 1). The decrease in median pore size (Fig. 4b) suggests a shift in the pore size distribution to smaller pores. This shift in the distribution of pore throat sizes during consolidation is quantitatively described with pore throat size probability density functions (Fig. 4c and d). The probability density function (PDF, in Fig. 4c and 4d) is the derivative of the cumulative porosity curve and thus the density function corresponds to the slopes of the cumulative curve. The probability density function is a measure of the relative abundance of pores for a given pore throat size.

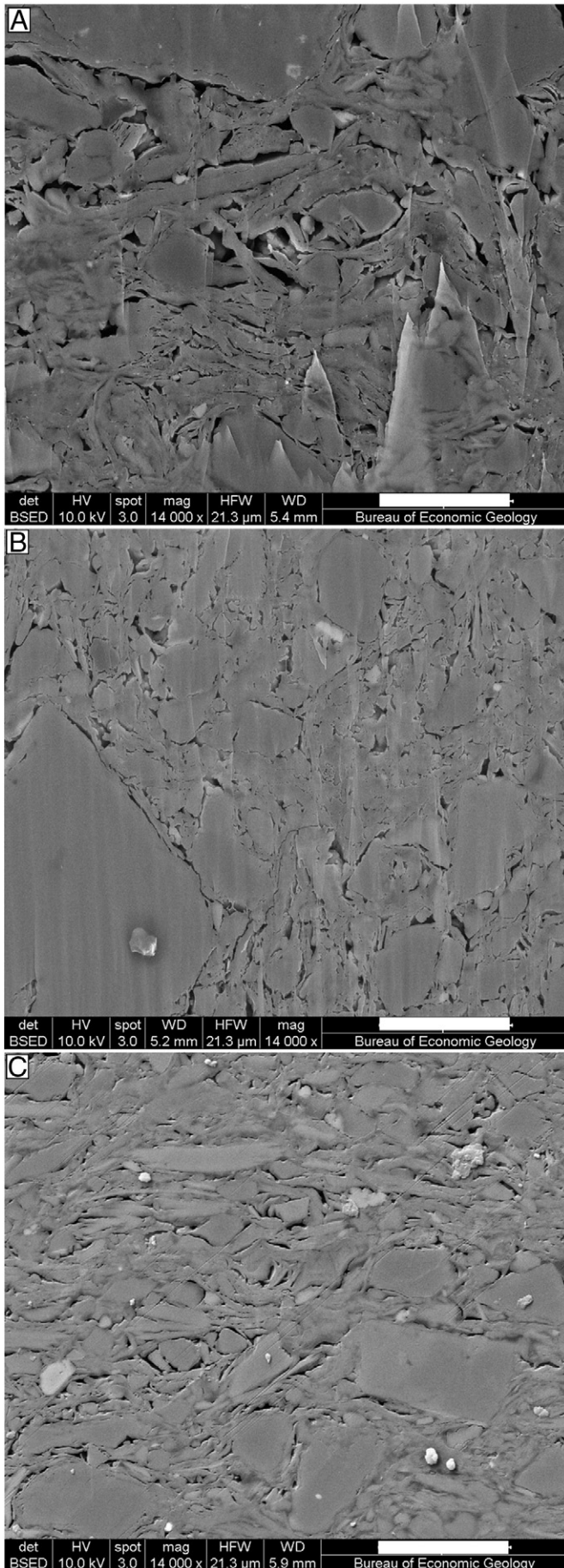
## 4. Discussion

### 4.1. Clay mineral rotation

Samples from Ursa allow a detailed study of the micro-fabric of mud-rich sediments from the shallow section. By removing the outlying data point at 579 mbsf a linear relationship between illite-smectite maximum pole density (m.r.d.) and vertical effective stress ( $\sigma_v$ ) is described by:

$$\text{m.r.d.} = 0.1903(\sigma_v) + 2.404 \quad (3)$$

where ( $\sigma_v$ ) is expressed in MPa (Fig. 5). The vertical effective stress ( $\sigma_v$ ) is derived from Table 1 in Flemings et al. (2008). Eq. (3) results



in a correlation coefficient of 0.67 and predicts that the maximum pole density (in m.r.d.) equals 2.40 at the seafloor where the vertical effective stress is zero. However, it is generally presumed that a flocculated clay aggregate is composed of randomly oriented clay particles (O'Brien, 1971) and thus has an "m.r.d." equal to 1. Alternatively, where void ratio ( $e = \text{porosity}/1 - \text{porosity}$ ) is correlated to fabric orientation lower maximum pole densities are predicted near the seafloor:

$$e = -0.44(\text{m.r.d.}) + 2.03 \quad (4)$$

In Eq. (4), the void ratio ( $e$ ) is calculated from logging while drilling porosity data (illustrated in Fig. 6) and a linear regression has a low correlation coefficient ( $r = 0.39$ ).

Long et al. (2011) related void ratio to effective stress in the Ursa Basin using:

$$1 + e = 1.89(\sigma_v')^{-0.0979} \quad (5)$$

where units of MPa are used for vertical effective stress ( $\sigma_v'$ ). Combining Eqs. (4) and (5) to predict a relationship between maximum pole density (m.r.d.) and vertical effective stress gives:

$$\text{m.r.d.} = 2.03 - \left[ \left( 1.89\sigma_v'^{-0.0979} \right) - 1 \right] / 0.44 \quad (6)$$

Eqs. (3) and (6) are illustrated in Fig. 7 along with recorded maximum pole densities. Eq. (6) predicts a lower "m.r.d." near the seafloor (~1.0) relative to Eq. (3) (m.r.d. = 2.40). Eq. (3) may be more applicable to data in the range 0.5 to 5.0 MPa of vertical effective stress where there is good agreement between the model and the measured data. Eq. (6) does a reasonable job approximating maximum pole density (m.r.d.) in the range of 0.0 to 4.0 MPa of vertical effective stress.

A more intuitive understanding of maximum pole density at very low vertical effective stresses, <0.25 MPa may be drawn from Eq. (6), as the inclusion of void ratio ( $e$ ) in its derivation links vertical effective stress to void ratio reduction. This paper does not explore the evolution of orientation at stresses higher than 4.0 MPa because higher stress samples were not available for study. However, at stresses beyond 4.0 MPa, both models have less predictive power. Eq. (3) predicts the maximum pole density in m.r.d. to be ~8 at 30 MPa, however values of 8 m.r.d. in burial settings are indicative of late-diagenesis to early metamorphism (Ho et al., 1999; Jacob et al., 2000; Day-Stirrat et al., 2008). In contrast, at 30 MPa Eq. (6) predicts the pole density in m.r.d. to be ~3.8, again lower than observed in previous studies. Although Eq. (6) is based on a weaker correlation coefficient, it may better describe the inability of clay minerals to form a strong preferred orientation as space (porosity) for clay particle rotation decreases before diagenetic clay mineral reactions become the dominant control on clay mineral preferred orientation. (Ho et al., 1999; Day-Stirrat et al., 2008).

#### 4.2. Pore throat size modification

To consolidate the samples at Ursa from 49% porosity to 31% porosity through an intermediate 37% porosity step, the largest pore throat sizes are relatively less abundant (Fig. 4b) and the relative abundance of small pores increases (Fig. 4c and d). One of the following three scenarios can cause this change during compression: 1) Small pores increase in abundance without changing large pores

**Fig. 3.** Backscattered electron images (A = 74.5 mbsf and  $\sigma_v' = 0.25$  MPa, B = 178.6 mbsf and  $\sigma_v' = 0.90$  MPa, C = 570.0 mbsf and  $\sigma_v' = 3.98$  MPa), on an Ar-ion milled surface, show large pores are preferentially lost with increasing vertical effective stress. Large pores (black areas) are preserved around the edges of silt size quartz grains. Scale bar is 5  $\mu\text{m}$  in each image.

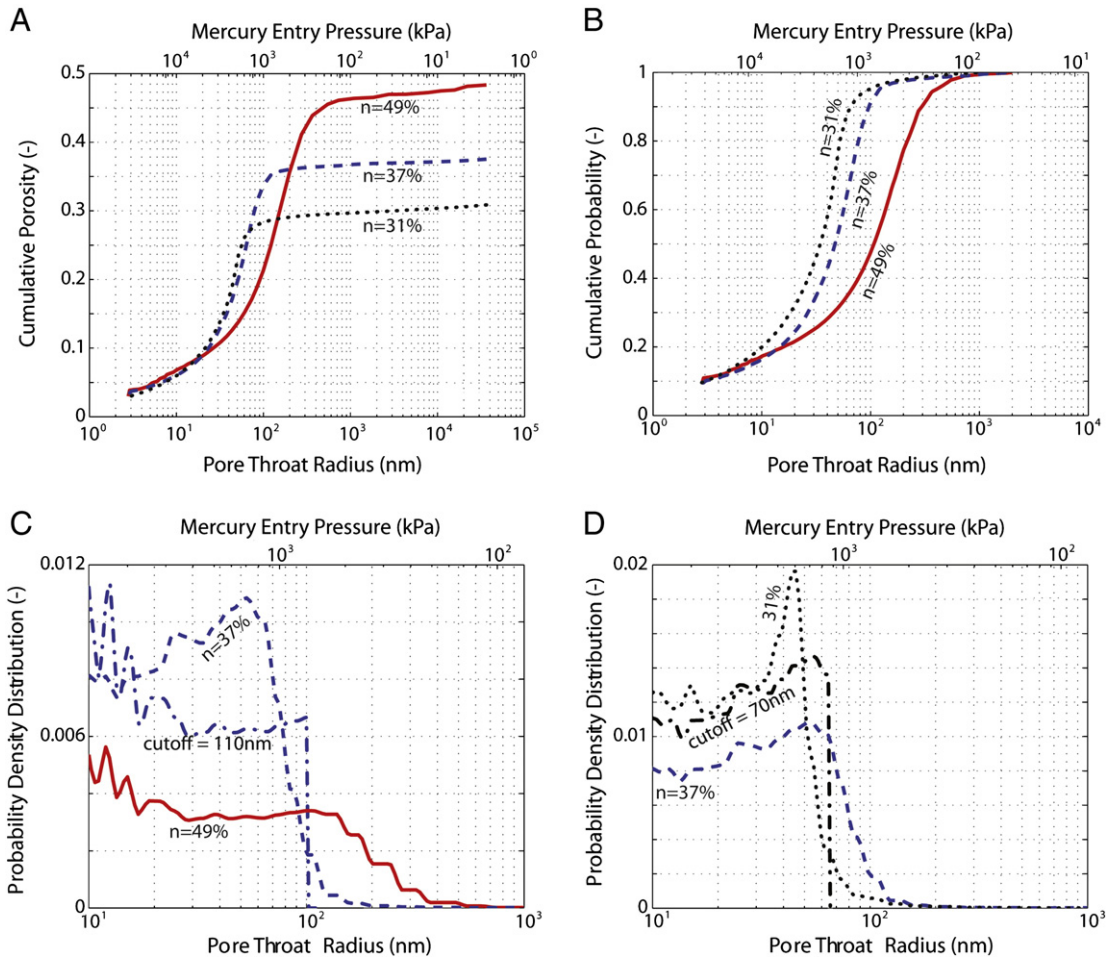


**Fig. 4.** Cumulative porosity curves (a) from mercury porosimetry for the samples imaged in A, B and C with their total porosities, 49%, 37% and 31% respectively. b) cumulative porosity curves for samples in b). Consolidation of samples from 49% to 37% porosity (c) does not evenly reduce pore throat radius or simply close off the largest pores. Large pore throats are lost > 110 nm and intermediate pore throats (10 to 110 nm) are created. The same trend is seen in reducing porosity from 37% to 31% (d) but the intermediate pore size range is reduced to 10 to 70 nm and no pore throats larger than 150 nm are present. In c) and d) we show the modeled probability density functions of large pore throats being cut off.

significantly; 2) Large pores are lost without changing small pores significantly; 3) Large pores are lost and we gain smaller pores from what were larger pores. Total porosity decreases with consolidation, therefore scenario 1) is not applicable. In the second case, a simple

model of closing these larger pores and then recalculating the new probability density function does not yield the recorded probability density function in our simulations. What follows is a modeling exercise to test this further Closing off pores larger than 110 nm and 70 nm in the 49% porosity sample (Fig. 4a,c and d) and recalculating

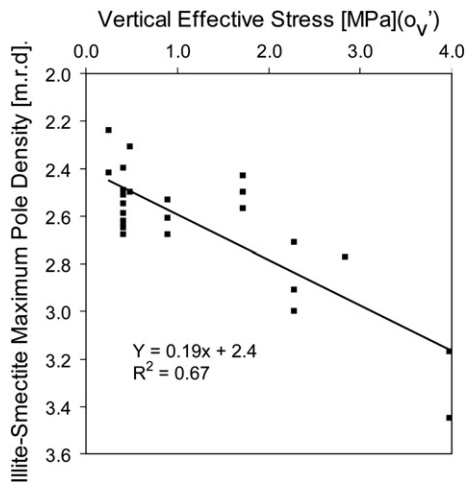


**Fig. 5.** The linear relationship between illite-smectite maximum pole density (preferred orientation) in multiples of a random distribution (m.r.d.) as a function of vertical effective stress (MPa). Vertical stress ( $\sigma_v'$ ) is derived from data in Flemings et al. (2008).

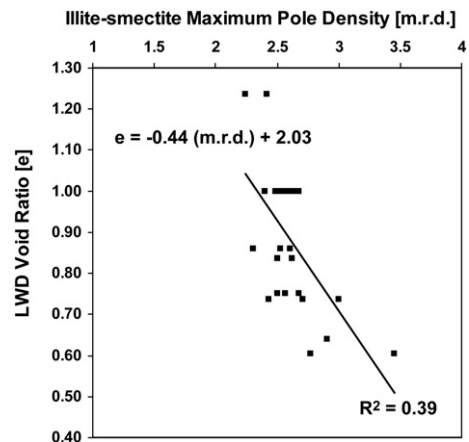


**Fig. 6.** The relationship between illite-smectite maximum pole density (preferred orientation) in multiples of a random distribution (m.r.d.) and the logging while drilling void ratio.

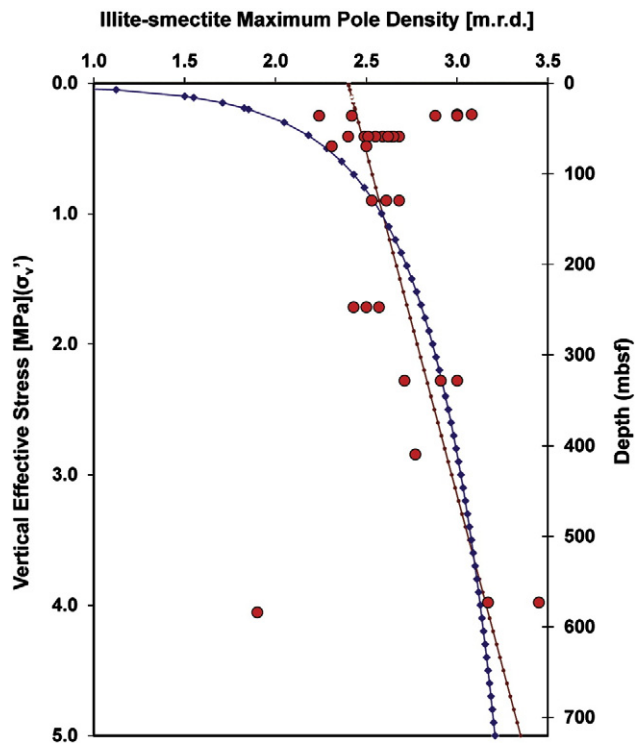


Fig. 7. Illite-smectite maximum pole density (m.r.d.) as a function of vertical effective stress ( $\sigma_v$ ). Straight line is linear regression shown in Fig. 3. Curved line predicts illite-smectite maximum pole density from logging while drilling void ratio (porosity) loss (Fig. 4) and increasing vertical effective stress by combining the Equation in Fig. 4 (Eq. (4)) with Eq. (5) (Long et al., 2011).

the probability density distribution for the model with 110 nm pore throat close off (total porosity is 25%) and 70 nm close off (total porosity is 19%) new total porosities are generated. By simply closing pore throats sizes larger than the largest pores encountered in our other *in-situ* samples it is not possible to generate either the probability density function or the total porosity (Fig. 4c and d). This finding appears contrary to other studies (Dewhurst et al., 1998; Dewhurst et al., 1999) where increased stress appeared to simply close off the largest pores. Therefore, modifying large pores into smaller pores must be the process occurring in our samples in both 49% to 37% and 37% to 31% porosity steps, with the median pore throat sizes decreasing in response to increased vertical effective stress. Indeed, clay mineral preferred orientations quantified here suggest that there is a fabric evolution occurring simultaneously with porosity loss.

Naturally, pore throat sizes generated by mercury porosimetry may not necessarily be representative of the entire pore distribution (Romero and Simms, 2008) and the possible effects of unconnected pores or pores connected by narrower throats than can be accessed given the mercury pressure conditions applied. However, pore size distributions in the range 5 nm to 400  $\mu\text{m}$  are reliable and describe and quantify the dominant pore size modes. By combining quantifications of mercury saturation data with high quality BSE images and X-ray diffraction defined clay mineral preferred orientation we are able to illuminate the pore fabric evolution with increasing vertical effective stress at Ursa

Field curves of consolidation have long been studied from the perspective of just the decline in porosity. The depth of our contribution is to relate the field curve of consolidation (Fig. 2), driven by the increase in vertical effective stress, to the wholesale fabric evolution of the mudstone at the pore and particle scale (Figs. 2, 6, and 7). The data demonstrates that the largest pore throats are preferentially associated with the larger grains (Fig. 4) and that larger pores are

preferentially lost and converted to intermediate pore sizes with increasing vertical effective stress. It is our interpretation that as a result of this process, there is a small but significant increase in the preferred orientation of (platy) clay grains in response to bulk mudstone fabric rearrangement and we are able to mathematically describe this as a function of porosity (void ratio) reduction.

## 5. Conclusions

Our clay mineral preferred orientation quantifications, pore size distribution and images are made on mudstones with a consistent grain size, ~65% clay sized (2  $\mu\text{m}$ ) particles and this paper note the following:

1. Porosity decreases, ~80 to ~35% over a 600 m measured section at Ursa.
2. Pore size distributions from MICP data define the loss of large pores with increasing consolidation and a reduction in median pore throat size.
3. Backscattered electron microscope images confirm this quantification and show the largest pores preferentially preserved around silt-sized quartz grains.
4. Pores become elongated with increasing vertical effective stress.
5. There is a small increase in clay mineral maximum pole density (preferred orientation) with increasing vertical effective stress.

The mechanical processes occurring in shallow buried mudstones significantly alter total porosity and pore size distributions and have a small effect on enhancing clay mineral fabric intensity in the first few hundred meters of burial. The highly aligned clay fabrics observed in some lithified mudstones, therefore, must result from processes other than solid particle rotation in response to continued vertical effective stress increase. Two simple models predict illite-smectite preferred orientation as a function of vertical effective stress; the first linearly relates the increase in illite-smectite preferred orientation to the increase in vertical effective stress with depth. The second model relates vertical effective stress, void ratio and illite-smectite preferred orientation and suggests that the rate of illite-smectite preferred orientation increase slows down at higher stresses as the space for particle rotation decreases.

## Acknowledgements

We thank the UT Geofluids industrial associates program for their sponsorship and the scientists of IODP Expedition Leg 308. This manuscript is published with the permission of the Director BEG, Scott Tinker Ph.D. MICP measurements were made at Newcastle University UK. HRXTG is supported by EMAL at the University of Michigan and NSF grant EAR-0345985 to Ben van der Pluijm. BSE images were prepared by Robert M. Reed. This research builds on insights derived from samples and/or data provided by the Integrated Ocean Drilling Program (IODP). The IODP is sponsored by the U.S. National Science Foundation (NSF) and participating countries. Emmanuel Simon, The Hebrew University in Jerusalem, is thanked for illuminating discussions.

## References

- Arch, J., Maltman, A., 1990. Anisotropic Permeability and Tortuosity in Deformed Wet Sediments. *Journal of Geophysical Research* 95, 9035–9045.
- Arnould, M., Audiguier, M., Delage, P., Pellerin, F.-M., Struillou, R., Vayssade, B., 1980. Etude des sols argileux par la porosimétrie au mercure. Contrôle des variations de texture sous diverses conditions. *International Association of Engineering Geologists Bulletin* 22, 213–223.
- Ask, M.V.S., Morgan, J.K., 2010. Projection of mechanical properties from shallow to greater depths seaward of the Nankai accretionary prism. *Tectonophysics* 482, 50–64.
- ASTM, 2007. Standard test method for particle-size analysis of soils. In: International, A. D 422–63. West Conshohocken, PA, p. 8.

- Athy, A.F., 1930. Density, porosity and compaction of sedimentary rocks. *AAPG Bulletin* 14, 1–24.
- Baldwin, B., Butler, C.O., 1985. Compaction Curves. *American Association of Petroleum Geologists Bulletin* 69, 622–626.
- Curtis, C.D., Lipshie, S.R., Oertel, G., Pearson, M.J., 1980. Clay Orientation in Some Upper Carboniferous Mudrocks, Its Relationship to Quartz Content and Some Inferences About Fissility, Porosity and Compactional History. *Sedimentology* 27, 333–339.
- Day-Stirrat, R.J., Aplin, A.C., Srodon, J., van der Pluijm, B.A., 2008. Diagenetic reorientation of phyllosilicate minerals in Paleogene mudstones of the Podhale Basin, southern Poland. *Clays and Clay Minerals* 56, 100–111.
- Day-Stirrat, R.J., Dutton, S.P., Milliken, K.L., Loucks, R.G., Aplin, A.C., Hillier, S., van der Pluijm, B.A., 2010. Fabric anisotropy induced by primary depositional variations in the silt: clay ratio in two fine-grained slope fan complexes: Texas Gulf Coast and northern North Sea. *Sedimentary Geology* 226, 42–53.
- Delage, P., Lefebvre, G., 1984. Study of the Structure of a Sensitive Champlain Clay and of Its Evolution During Consolidation. *Canadian Geotechnical Journal* 21, 21–35.
- Dewhurst, D.N., Aplin, A.C., Sarda, J.P., Yang, Y.L., 1998. Compaction-driven evolution of porosity and permeability in natural mudstones: An experimental study. *Journal of Geophysical Research-Solid Earth* 103, 651–661.
- Dewhurst, D.N., Yang, Y., Aplin, A.C., 1999. Permeability and fluid flow in natural mudstones. *Geological Society, London, Special Publications* 158, 23–43.
- Domnesteanu, P., McCann, C., Sothcott, J., 2002. Velocity anisotropy and attenuation of shale in under- and overpressured conditions. *Geophysical Prospecting* 50, 487–503.
- Flemings, P.B., Behrmann, J.H., John, C.M., the Expedition 308 Scientists, 2006. Proc. IODP, 308: College Station TX (Integrated Ocean Drilling Program Management International, Inc.). doi:10.2204/iodp.proc.308.101.2006.
- Flemings, P.B., Long, H., Dugan, B., Germaine, J., John, C.M., Behrmann, J.H., Sawyer, D., Scientists, I.E., 2008. Erratum to "Pore pressure penetrometers document high overpressure near the seafloor where multiple submarine landslides have occurred on the continental slope, offshore Louisiana, Gulf of Mexico" (vol 269, pg 309, 2008). *Earth and Planetary Science Letters* 274, 269–283.
- Forsberg, C.F., Locat, J., 2005. Mineralogical and microstructural development of the sediments on the Mid-Norwegian margin. *Marine and Petroleum Geology* 22 (1–2), 109–122.
- Hart, B.S., Flemings, P.B., Deshpande, A., 1995. Porosity and Pressure - Role of Compaction Disequilibrium in the Development of Geopressures in a Gulf-Coast Pleistocene Basin. *Geology* 23, 45–48.
- Hedberg, H.D., 1936. Gravitational compaction of clays and shales. *American Journal of Sciences* 31, 241–287.
- Hildenbrand, A., Urai, J.L., 2003. Investigations of the morphology of pore space in mudstones—first results. *Marine and Petroleum Geology* 20, 1185–1200.
- Ho, N.C., Peacor, D.R., van der Pluijm, B.A., 1999. Preferred Orientation of Phyllosilicates in Gulf Coast Mudstones and Relation to the Smectite-Illite Transition. *Clays and Clay Minerals* 47, 495–504.
- Jacob, G., Kisch, H.J., van der Pluijm, B.A., 2000. The relationship of phyllosilicate orientation, X-ray diffraction intensity ratios, and c/b fissility ratios in metasedimentary rocks of the Helvetic zone of the Swiss Alps and the Caledonides of Jamtland, central western Sweden. *Journal of Structural Geology* 22, 245–258.
- John, C.M., Adatte, T., 2009. Data report: X-ray analyses of bulk sediment in IODP Holes U1320A and U1324B, northern Gulf of Mexico. In: Flemings, P.B., Behrmann, J.H., John, C.M., the Expedition 308 Scientists (Eds.), Proc. IODP 308. Integrated Ocean Drilling Program Management International, Inc., College Station, TX.
- Long, H., Flemings, P.B., Germaine, J.T., Saffer, D.M., 2011. Consolidation and overpressure near the seafloor in the Ursa Basin, Deepwater Gulf of Mexico. *Earth and Planetary Science Letters* 305, 11–20.
- Loucks, R.G., Reed, R.M., Ruppel, S.C., Jarvie, D.M., 2009. Morphology, Genesis, and Distribution of Nanometer-Scale Pores in Siliceous Mudstones of the Mississippian Barnett Shale. *Journal of Sedimentary Research* 79, 848–861.
- Lowell, S., Shields, J.E., 1984. Powder Surface Area and Porosity, second ed. Wiley, New York.
- O'Brien, N.R., 1971. Fabric of Kaolinite and Illite Floccules. *Clays and Clay Minerals* 19, 353–359.
- Romero, E., Simms, P., 2008. Microstructure Investigation in Unsaturated Soils: A Review with Special Attention to Contribution of Mercury Intrusion Porosimetry and Environmental Scanning Electron Microscopy. *Geotechnical and Geological Engineering* 26, 705–727.
- Rubey, W.W., Hubbert, M.K., 1959. Overthrust belt geosynclinal area western Wyoming in light of fluid-pressure hypothesis, 2) Role of fluidpressure in mechanics of overthrust faulting. *Geological Society of America Bulletin* 70, 167–205.
- Sawyer, D.E., Jacoby, R., Flemings, P.B., Germaine, J.T., 2008. Data Report: Particle Size Analysis of Sediments in the Ursa Basin, IODP Expedition 308 Site U1324 and U1322, Northern Gulf of Mexico. In: Flemings, P.B., John, C. (Eds.), Proc. ODP, Sci. Results, 308.
- Sawyer, D.E., Flemings, P.B., Dugan, B., Germaine, J.T., 2009. Retrogressive failures recorded in mass transport deposits in the Ursa Basin, Northern Gulf of Mexico. *Journal of Geophysical Research-Solid Earth* 114.
- Schowalter, T.T., 1979. Mechanics of Secondary Hydrocarbon Migration and Entrapment. *American Association of Petroleum Geologists Bulletin* 63, 723–760.
- Slater, J.C., Christie, P.A.F., 1980. Continental Stretching - an Explanation of the Post-Mid-Cretaceous Subsidence of the Central North-Sea Basin. *Journal of Geophysical Research* 85, 3711–3739.
- Sintubin, M., 1995. High-resolution X-ray texture goniometry: Discussion. *Journal of Structural Geology* 17, 923–924.
- Solum, J.G., van der Pluijm, B.A., 2009. Quantification of fabrics in clay gouge from the Carboneras fault, Spain and implications for fault behavior. *Tectonophysics* 475, 554–562.
- Solum, J.G., van der Pluijm, B.A., Peacor, D.R., 2005. Neocrystallization, fabrics and age of clay minerals from an exposure of the Moab Fault, Utah. *Journal of Structural Geology* 27, 1563–1576.
- van der Pluijm, B.A., Ho, N.-C., Peacor, D.R., 1994. High-resolution X-ray texture goniometry. *Journal of Structural Geology* 16, 1029–1032.
- van der Pluijm, B.A., Ho, N.-C., Peacor, D.R., 1995. High-resolution X-ray texture goniometry: Reply. *Journal of Structural Geology* 17, 925–926.
- Wenk, H.R., 1985. Measurement of pole figures. In: Wenk, H.R. (Ed.), Preferred orientation in deformed metals and rocks: An introduction to modern texture analysis. Academic Press, INC., pp. 11–48.